KRONOS FUSION ENERGY

PAPER 2.41 · THE KRONOS 2026 SERIES

Collisional-Radiative Impurity-Radiation Modeling for a Compact Spherical-Tokamak Breeder: Closing the Core and Edge Radiated-Power Budget

The radiated-power ledger is what keeps a first-wall material honest: every watt an impurity radiates from the core is a watt subtracted from the fusion power balance, and every...

Read it live — 3-D model · physics validator · film series

BY P I FORD AND G L KULCINSKI

2026 · EDITORIAL EDITION

THE OFFICIAL RECORD

What this document is, and how to read its numbers

This is a combined editorial. It gathers, in one volume, the two design studies Kronos Fusion Energy released in 2026 — a compact spherical-tokamak tritium/helium-3 breeder and a deuterium–helium-3 tandem-mirror generator — together with the intellectual-property estate, the people, and, in the internal edition, the full commercial case. The scientific text is the same text that appears in the arXiv preprints and the journal submissions; the editorial adds the apparatus a reader needs to hold the whole program at once, and nothing in the physics is altered to fit it.

THE HONESTY STANCE IS THE ASSET

Every headline quantity carries an **evidence class** — DERIVED RECOMPUTED MEASURED REQUIREMENT — and, where a number is a modelled extrapolation rather than a demonstrated value, it is labelled as such and its downside is shown next to it. Several quantities in the underlying corpus moved after first publication; where a value has been withdrawn or restated, the record says so plainly. This is deliberate: a diligence team will find the load-bearing assumptions, so the document surfaces them first.

TWO EDITIONS

This volume is issued in two editions. The **public edition** (light) carries the physics and the design only — no dollar, price, or per-kilogram figure appears anywhere in it. The **internal edition** (dark) adds the economics, the funding architecture, and the defense-commercial analysis, and is marked *Confidential* accordingly; it is not for public distribution. Where the commercial case rests on a modelled assumption rather than a demonstrated one, it is labelled as such and its downside is shown alongside it, on the same terms as the physics.

TITLE	The Kronos Fleet — Hyperion · Aegis · MetroVolt: A Combined Design & Commercialization Study
AUTHOR	Priyanca Ford, Founder & CEO, on behalf of Kronos Fusion Energy
EDITION	2026 Combined Editorial · first issue
COMPANION WORKS	The five-paper arXiv drop — (1) Breeder, (2) Burner, (3) REBCO magnet & tape, (4) Direct Energy Conversion, (5) AI/ML/Quantum control — with matching numbered Zenodo deposits, plus the IOP journal and IAEA-FEC submissions. Patents were filed before the drop.
NAMING	Hyperion = the breeder; Aegis (defense) and MetroVolt (data-center) = one generator in two housings. Internal mode letters (D1, L) do not appear on public surfaces.
STATUS	Conceptual design & simulation study. Nothing herein is a construction commitment.

HOW TO READ THIS VOLUME

The fleet at a glance, and the way its numbers are marked

This volume opens with *Orientation*, presents the five research papers as a bound sequence, and closes with the *Apparatus*. *Foundations* sets out the three general results both machines rest on. *Paper One* is the Hyperion breeder; *Paper Two* the Aegis / MetroVolt generator; *Papers Three, Four and Five* are the enabling science — high-field REBCO magnets and tape, direct energy conversion, and the AI / ML / quantum control stack. A *Digital Twin & 3-D Model* part follows, then the *Environmental* profile. The *Economics* and levelized cost and the *Business Case* and diligence record appear in the internal edition only; the *Simulations* proof record and the Apparatus — patent portfolio, team, limitations, and sources — close both editions.

THE FLEET AT A GLANCE

	HYPERION	AEGIS	METROVOLT
Role	Strategic-isotope foundry	Defense installation power	Campus power
Machine	**Spherical tokamak**	**Tandem mirror**	**Tandem mirror**
Fuel	Deuterium–tritium	Deuterium–helium-3	Deuterium–helium-3
Delivers	Tritium · ^{3}He · 14 MeV n	Resilient installation power	Firm campus power
Physics bar	**Fusion gain only**	Closure (gates named)	Closure + lunar ^{3}He
In the fleet	Breeds the fuel	Proves the generator	Commercial destination

HOW THE NUMBERS ARE MARKED

Every headline quantity carries an evidence class — DERIVED from first principles, RECOMPUTED from raw data, MEASURED in hardware, or a REQUIREMENT yet to be met. Financial figures carry a case label and are confined to the internal (confidential) edition. Values that moved after first publication are shown as withdrawn or restated rather than quietly changed. A capability you can evaluate is one whose limits are on the page.

ABSTRACT

Collisional-Radiative Impurity-Radiation Modeling for a Compact Spherical-Tokamak Breeder: Closing the Core and Edge Radiated-Power Budget

The radiated-power ledger is what keeps a first-wall material honest: every watt an impurity radiates from the core is a watt subtracted from the fusion power balance, and every watt radiated at the edge is a watt usefully removed from the exhaust. For a compact, high-power-density spherical-tokamak breeder armoured in tungsten—the right plasma-facing material and the worst possible core contaminant—this trade must be quantified, not assumed. We formalise the radiated-power budget as a collisional-radiative (CR) problem and solve it for the frozen Hyperion breeder operating point ($P_{\text{fus}} = 85.04\,MW$, $Q = 3.076$, $I_p = 9.66\,MA$, core $T_e = 15\,keV$, $n_e = 4.0e20\,/m^3$ at Greenwald fraction 0.30, plasma volume $10.9\,m^3$). Under a coronal-equilibrium charge-state balance evaluated from OpenADAS ADF11 radiated-power coefficients, we compute the cooling factor $L_z(T_e)$ and mean charge $\langle Z\rangle(T_e)$ for tungsten and argon across a $1\,eV$–$50\,keV$ grid, so the core is evaluated directly with no extrapolation. Tungsten radiates at $L_z = 5.70e-32\,Wm^3$ in the $15\,keV$ core with $\langle Z\rangle = 61.9$, rising through a broad maximum ($2.05e-31\,Wm^3$) near $1\,keV$; argon is two orders of magnitude weaker in the core but radiates $\approx 13\times$ harder at the $100\,eV$ edge, the signature of a benign edge radiator. An independent ADAS hydrogenic route reproduces the register bremsstrahlung power to within 10–$20\,\%$, confirming the $P_{\text{rad}} = 4.67\,MW$ hydrogenic budget ($P_{\text{brems}} = 3.117\,MW$, $P_{\text{sync}} = 1.553\,MW$, $Z_{\text{eff}} = 1.158$) by a route sharing none of its assumptions. Profile-integrating the CR emissivity converts the curves into an engineering specification: a **tungsten tolerance of $\approx 0.19\,MW$ per ppm**. Holding core tungsten at or below $3\,ppm$ keeps the impurity add-on under $0.6\,MW$ ($< 13\,\%$ of budget), whereas an uncontrolled $42\,ppm$ would nearly triple total radiation; the same Z_{eff} excursion carried by argon adds a tolerable, edge-weighted $\approx 1.8\,MW$. The curves close the radiation bookkeeping and set a quantitative core-purity budget that a divertor and impurity-screening design is built to deliver.

Open-access deposit (code & data, CC BY 4.0): DOI 10.5281/zenodo.22645883 · Zenodo community *kronos_fusion_energy*. Explore it live: interactive 3-D model · physics validator.

Keywords: radiated power · collisional-radiative modelling · impurity radiation · tungsten · argon · ADAS · coronal equilibrium · spherical-tokamak breeder

CONTENTS

Table of Contents

NOMENCLATURE

Symbols, units, and the names of things

Q	plasma (fusion) gain, P_{fus}/P_{aux}
Q_E	engineering gain, net electric out / recirculating in
H_{98}	confinement enhancement over the IPB98(y,2) scaling
Z_{eff}	effective ion charge
c_{ee}	electron–electron bremsstrahlung leading coefficient, 2.120022 (exact)
τ_E	energy confinement time
I_p	plasma current
R_0, a	major radius, minor radius
κ, δ	elongation, triangularity
β_N	normalized plasma beta (Troyon-normalized)
TBR	tritium breeding ratio
DEC	direct energy conversion
CF	plant capacity factor (availability)
FOAK / NOAK / BOAK	first / n^{th} / best of a kind
Hyperion	the ST breeder (internal: Mode D2)
Aegis	the generator, defense/installation housing (internal: Mode M)
MetroVolt	the generator, data-center housing (Mode M)

§ 1

Introduction

Radiation is the one loss channel a magnetic-confinement plasma cannot switch off. Line and continuum emission from partially-stripped impurities is at once the plasma's most dangerous core loss and its most useful edge tool: the same atomic physics that erodes central confinement when a heavy ion reaches the core is what spreads the divertor exhaust when a light ion is deliberately seeded at the edge [12,13]. A device that must run a tungsten first wall lives on the sharp side of that trade, because tungsten is simultaneously the reference plasma-facing material—for its high sputtering threshold, low tritium retention and thermomechanical margin [16,17]—and, at $Z = 74$, the impurity that radiates hardest per nucleus. Getting the radiated-power ledger right is therefore not a refinement; it is a precondition for claiming that a tungsten-walled machine can hold its power balance at all.

The machine in question is the Hyperion breeder, a compact low-aspect-ratio spherical tokamak ($R_0 = 1.20\,m$, aspect ratio $A = 2.5$, elongation $\kappa = 2.0$, negative triangularity $\delta = -0.30$, $B_0 = 8\,T$, centrepost peak field $16.84\,T$) sized to a strategic-isotope mission rather than a net-electric optimum. Its ratified design point sits on the $Q = 3.076$ contour at $P_{\text{fus}} = 85.04\,MW$ and $I_p = 9.66\,MA$, a self-heated, well-conditioned regime whose product is tritium, helium-3 and 14 MeV neutrons. The compact, high-field, spherical-tokamak class it belongs to—exemplified by the pilot-plant studies of Menard *et al.* [19], the high-field ARC line [20] and the SPARC tokamak [21]—pushes power density up, which sharpens every exhaust and radiation constraint at once. The negative-triangularity shape brings a genuine benefit on the confinement side by suppressing edge-localised turbulence [22,23]; it does nothing to relax the atomic physics of radiation, which is set by temperature, density and charge state alone.

The atomic-data foundation for radiated-power modelling is mature. Steady-state coronal cooling rates for the elements were tabulated by Post *et al.* [1]; the generalised collisional-radiative formalism and its practical implementation are the Atomic Data and Analysis Structure (ADAS) [2]; consistent tungsten cooling factors were computed and benchmarked against tokamak measurements by P\"utterich *et al.* [3], who later derived tolerable impurity concentrations for a reactor from a self-consistent cooling-factor set [4]; and compact polynomial fits of the coronal rates for eleven elements including tungsten are given by Mavrin [5,6]. Open-source solvers—ColRadPy [7] for the CR and ionisation balance, and radas [8] for OpenADAS-driven cooling-curve generation—make the calculation reproducible. What that literature does not provide is a *machine-specific* ledger: the numbers that close a particular device's radiated-power budget and turn its cooling curves into a purity specification its divertor and impurity-screening systems must meet.

This paper computes that ledger for the frozen Hyperion operating point and states it as mathematics. Our contributions are four. (i) We cast the radiated-power budget as a formal CR problem—the ionisation-balance rate system, its coronal reduction, the cooling-factor functional and the continuum terms—and give the discretisation and solver used to evaluate it (Sec. 2–3). (ii) We compute $L_z(T_e)$ and $\langle Z\rangle(T_e)$ for tungsten and argon on a grid that brackets the core with no extrapolation, obtaining the frozen anchor $L_z^{\mathrm{W}}(15\,keV) = 5.70e-32\,Wm^3$ (Sec. 4.1). (iii) We confirm the hydrogenic radiation budget $P_{\text{rad}} = 4.67\,MW$ by an independent ADAS route that shares none of the transport model's assumptions, closing to within 10–$20\,\%$ (Sec. 4.2). (iv) We profile-integrate the CR emissivity to a single engineering number—a tungsten tolerance of $\approx 0.19\,MW$ per ppm, hence a core-purity specification of $\leq 3\,ppm$—and show the same Z_{eff} excursion carried by argon is a tolerable, edge-weighted addition (Sec. 4.2–4). Every quantitative claim traces to the collisional-radiative run in the Kronos physics de-risking campaign (serial BR-L2-A29), cross-checked against the radiation-transport run (serial KX-L1-A3), and is archived in the de-risking register [32]. The result complements the companion neoclassical impurity-screening analysis [26], the radiative-boundary density-limit map [28], and the divertor detachment portfolio [30,31] that together determine whether the few-ppm target this paper sets can be delivered.

§ 2

Governing equations and the formal radiated-power problem

We define the radiated-power budget from the impurity charge-state kinetics upward, so that every reported number has an equation behind it. Throughout, T_e is the electron temperature, n_e the electron density, and an impurity species of nuclear charge Z is resolved into charge states $q = 0, 1, \ldots, Z$ with densities $n_z^{(q)}$ and total density $n_z = \sum_q n_z^{(q)}$.

THE COLLISIONAL-RADIATIVE RATE SYSTEM

In a finite-density plasma the population of each charge state is governed by a collisional-radiative (CR) balance between electron-impact ionisation, radiative and dielectronic recombination, three-body recombination, and—at the fine-structure level folded into the CR coefficients—excitation and spontaneous emission [2]. Writing the ground-state-resolved, CR-collapsed coefficients as the ionisation rate $S^{(q)}(T_e, n_e)$ (state $q \to q+1$) and the total recombination rate $\alpha^{(q)}(T_e, n_e)$ (state $q \to q-1$), the charge-state densities evolve as

$$\frac{\partial n_z^{(q)}}{\partial t} = n_e \Big[S^{(q-1)} n_z^{(q-1)} - \big(S^{(q)} + \alpha^{(q)}\big)\, n_z^{(q)} + \alpha^{(q+1)} n_z^{(q+1)} \Big] + \nabla\cdot\big(D\,\nabla n_z^{(q)} - \quad v\, n_z^{(q)}\big),$$

with $S^{(-1)} \equiv \alpha^{(0)} \equiv S^{(Z)} \equiv \alpha^{(Z+1)} \equiv 0$. The final divergence term collects classical and turbulent impurity transport with diffusivity D and pinch velocity v; its magnitude relative to the local ionisation/recombination frequencies sets whether the charge-state distribution is in equilibrium. Collecting the state vector $n = (n_z^{(0)}, \ldots, n_z^{(Z)})^\top$, the reaction part of Eq. 1 is linear,

$$\dot{} \; n = n_e\, \mathsf{A}(T_e, n_e) \quad n + (\text{transport}), \qquad \mathsf{A} = \begin{pmatrix} -S^{(0)} & \alpha^{(1)} & & \\ S^{(0)} & -\big(S^{(1)}+\alpha^{(1)}\big) & \alpha^{(2)} & \\ & S^{(1)} & \ddots & \ddots \\ & & \ddots & -\alpha^{(Z)} \end{pmatrix},$$

a tridiagonal, column-conservative rate matrix ($\sum_q \dot{n}_z^{(q)} = 0$ in the absence of transport), which is the structure exploited by the numerical solver of Sec. 3.

CORONAL EQUILIBRIUM AND THE COOLING FACTOR

In the hot, tenuous core of a magnetic-confinement plasma the ionisation and recombination frequencies vastly exceed both the transport frequency and the three-body recombination rate ($\propto n_e$), so Eq. 1 relaxes to *coronal equilibrium*: a detailed balance in which each adjacent pair of charge states is separately stationary,

$$S^{(q)}(T_e)\, n_z^{(q)} = \alpha^{(q+1)}(T_e)\, n_z^{(q+1)}.$$

The fractional abundances $f^{(q)} \equiv n_z^{(q)}/n_z$ then follow the density-independent recursion

$$\frac{f^{(q+1)}}{f^{(q)}} = \frac{S^{(q)}(T_e)}{\alpha^{(q+1)}(T_e)}, \qquad f^{(q)}(T_e) = \frac{\prod_{j=0}^{q-1} \big[S^{(j)}/\alpha^{(j+1)}\big]}{\sum_{k=0}^{Z} \prod_{j=0}^{k-1} \big[S^{(j)}/\alpha^{(j+1)}\big]}, \qquad \sum_q f^{(q)} = 1.$$

Figure 1 sketches the balance. Because Eq. 4 depends only on temperature, coronal L_z is a function of T_e alone—the property that makes it the natural currency of a radiated-power budget. The radiated-power density of the species is the sum over charge states of the ADF11 line-power (P_{LT}) and recombination-plus-bremsstrahlung continuum (P_{PRB}) coefficients weighted by the fractional abundances,

$$P_{\mathrm{rad}}^{\mathrm{imp}} = n_e\, n_z\, L_z(T_e), \qquad L_z(T_e) = \sum_{q=0}^{Z} f^{(q)}(T_e) \Big[P_{\mathrm{LT}}^{(q)}(T_e) + P_{\mathrm{PRB}}^{(q)}(T_e) \Big],$$

which *defines* the cooling factor L_z (units $\mathrm{W\,m^3}$). The corresponding mean charge state, which sets both the effective charge the impurity contributes and how completely it is stripped, is

$$\langle Z\rangle(T_e) = \sum_{q=0}^{Z} q\, f^{(q)}(T_e), \qquad \langle Z^2\rangle(T_e) = \sum_{q=0}^{Z} q^2 f^{(q)}(T_e).$$

Equations 4–6 are the entire coronal model: given ADF11 coefficients they return $L_z(T_e)$ and $\langle Z\rangle(T_e)$ with no free parameters.

CONTINUUM RADIATION: BREMSSTRAHLUNG AND SYNCHROTRON

The hydrogenic background—the D/T fuel and its helium ash—radiates through two continuum channels that carry no impurity line power and are therefore accounted separately. Electron–ion bremsstrahlung integrates the relativistic, Gaunt-corrected emissivity over a Maxwellian to the compact form used in the register,

[redacted]

with T_e in keV and densities in $/m^3$; Z_{eff} is the line-averaged effective charge, here carried entirely by the fuel-ash mix ($Z_{\text{eff}} = 1.158$). Synchrotron (electron-cyclotron) emission, strongly reabsorbed and wall-reflected, follows the Trubnikov/Albajar scaling [10]

$$p_{\text{sync}} \;\propto\; n_e\, T_e\, B^2\,(1 - R_w)\, \Phi\big(T_e,\, B,\, a,\, R_w\big),$$

where B is the field, R_w the wall reflectivity and Φ a dimensionless optical-depth factor that folds in geometry and reabsorption. The total hydrogenic radiated power is the volume integral $P_{\text{rad}} = \int_V (p_{\text{brems}} + p_{\text{sync}})\, \mathrm{d}V$, evaluated by the CYTRAN-class transport solver of serial KX-L1-A3 to $P_{\text{brems}} = 3.117\, MW$ and $P_{\text{sync}} = 1.553\, MW$, i.e. $P_{\text{rad}} = 4.670\, MW$. This budget contains *no* impurity line radiation by construction; the CR model of Sec. 2.2 supplies exactly that missing piece.

PROFILE-INTEGRATED IMPURITY POWER AND THE TOLERANCE FUNCTIONAL

An impurity of concentration $c_z \equiv n_z/n_e$ (assumed radially uniform, the conservative worst case for a core contaminant) adds a radiated power obtained by integrating Eq. 5 over the plasma volume against the temperature profile,

$$P_{\text{imp}}[c_z] = \int_V n_e(r)\, n_z(r)\, L_z\big(T_e(r)\big)\, \mathrm{d}V = c_z \int_V n_e^2(r)\, L_z\big(T_e(r)\big)\, \mathrm{d}V.$$

Because Eq. 9 is linear in c_z, the impurity radiated power is fixed by a single species-dependent *tolerance functional*

$$\frac{\mathrm{d}P_{\text{imp}}}{\mathrm{d}c_z} = \int_V n_e^2(r)\, L_z\big(T_e(r)\big)\, \mathrm{d}V \;\equiv\; \mathcal{S}_z,$$

the megawatt-per-unit-concentration slope. Evaluating Eq. 10 on the frozen plasma model of Sec. 3 for tungsten yields the headline sensitivity $\mathcal{S}_{\text{W}} \approx 0.19\, MW$ per ppm; the admissible core concentration is then the largest c_z satisfying a chosen budget fraction η,

$$c_z^{\max} = \frac{\eta\, P_{\text{rad}}}{\mathcal{S}_z}, \qquad c_{\text{W}}^{\max}\big|_{\eta=0.13} \;\approx\; 3\; ppm.$$

Equation 11 is the core-purity specification: a design requirement stated as an inequality on a single measurable quantity.

THE EFFECTIVE-CHARGE PARTITION PROBLEM

A second, complementary constraint fixes how much of a given Z_{eff} excursion each species can carry. From the definition in Eq. 7, a uniform impurity at concentration c_z raises the effective charge by

$$\Delta Z_{\text{eff}} = c_z\, \big[\langle Z^2\rangle - \langle Z\rangle\big](T_e),$$

so a prescribed excursion $\Delta Z_{\text{eff}} = 0.158$ (the value carried by the fuel-ash mix in the register) maps to a species concentration $c_z = \Delta Z_{\text{eff}}/[\langle Z^2\rangle - \langle Z\rangle]$. Substituting into Eq. 9 gives the radiated power the *same* charge excursion would cost if it were carried by argon versus tungsten—the comparison at the heart of the core-purity argument (Sec. 4.2). The two constraints, Eqs. 11 and 12, are the formal problem this paper solves.

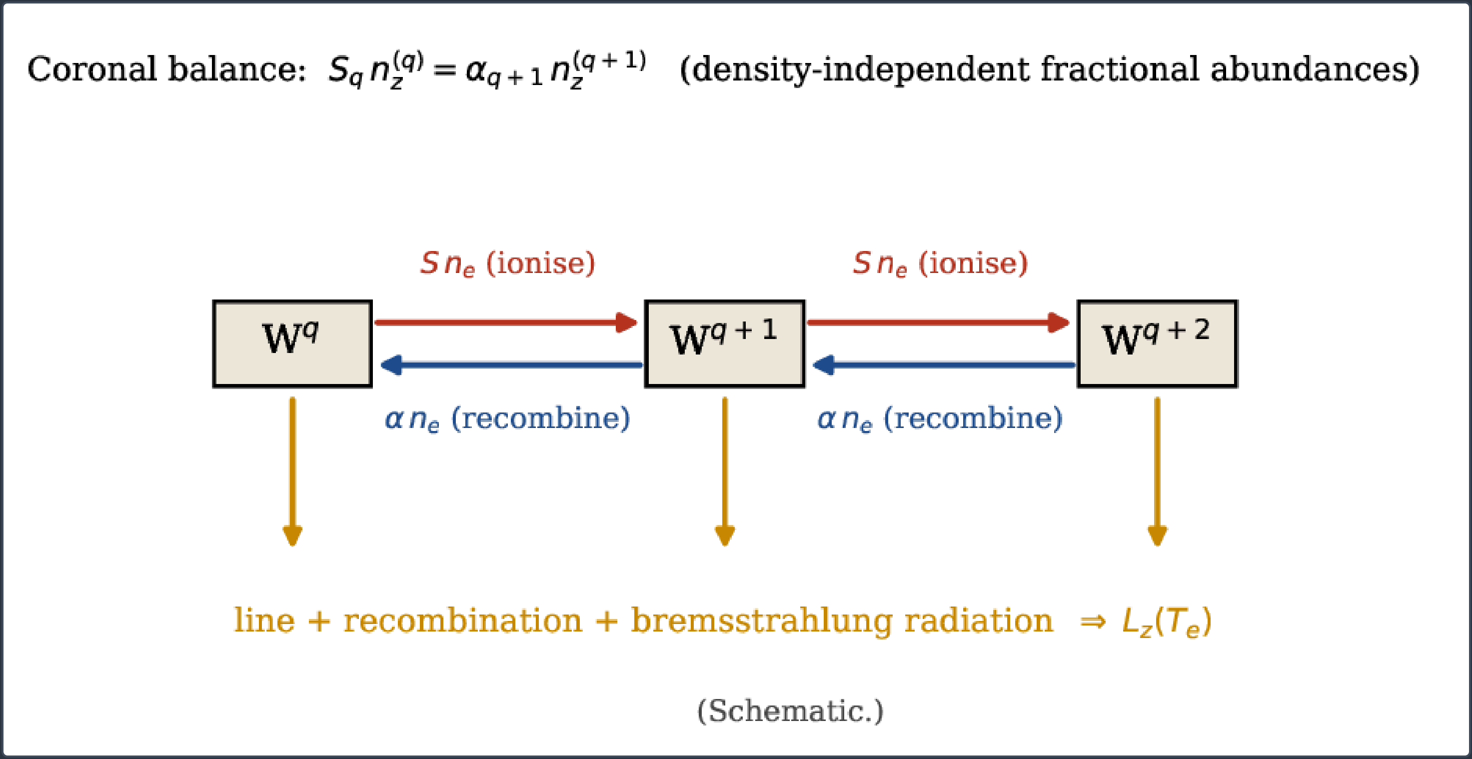

(Schematic.) The coronal charge-state balance underlying Eqs. 3–5: electron-impact ionisation ($S\,n_e$, forward) is balanced against radiative/dielectronic recombination ($\alpha\,n_e$, backward) state by state, and the residual line, recombination and bremsstrahlung emission is collected into the cooling factor $L_z(T_e)$. In coronal equilibrium the fractional abundances—and hence L_z—depend on temperature alone.

§ 3

Computational methodology: the GPU HPC campaign

The numbers in Sec. 2 were produced by a dedicated run of the Kronos physics de-risking campaign on the NVIDIA GPU HPC platform. This section names the codes, the discretisation, the convergence controls and the reproducibility protocol, so that the results are regenerable.

CODES AND ATOMIC DATA

The cooling curves were generated with radas [8], which ingests OpenADAS ADF11 radiated-power coefficients (line power P_{LT} and recombination/bremsstrahlung continuum P_{PRB}, year-89 data), solves the coronal ionisation balance of Eq. 4, and evaluates L_z and $\langle Z\rangle$ via Eqs. 5–6. The ground-state-resolved CR reduction that underlies the ADF11 coefficients is the generalised collisional-radiative model of Summers *et al.* [2]; where a fully density-resolved balance was wanted for verification, the same charge-state system, Eq. 2, was solved with ColRadPy [7]. The hydrogenic continuum budget and its synchrotron reabsorption were computed by the KRONOS Toolkit CYTRAN-class radiation-transport solver (serial KX-L1-A3), independent of the ADAS route, so that the two cross-check each other in Sec. 4.2. All atomic data are drawn from the public OpenADAS distribution; the tungsten coefficients are consistent with the benchmarked set of P\"utterich *et al.* [3].

DISCRETISATION AND SOLVER

The temperature axis is discretised on a logarithmic grid spanning $1\,eV$ to $50\,keV$ ($N_T = 200$ points, $\Delta\log_{10}T_e \approx 0.023$), chosen so that the $15\,keV$ core lies interior to the grid and is evaluated by direct table lookup with *no* extrapolation. A parallel density axis spans $1e16$ to $1e21\,/m^3$ to expose the finite-density sensitivity of Sec. 4. ADF11 coefficients are interpolated bicubically in $(\log T_e, \log n_e)$. At each grid node the coronal recursion Eq. 4 is evaluated as a running product with running renormalisation to preserve $\sum_q f^{(q)} = 1$ to machine precision; where the full CR matrix Eq. 2 is used, its null space (the stationary distribution) is obtained by a sparse tridiagonal solve, which is exact for the bidiagonal-plus-diagonal structure and avoids the ill-conditioning of a dense eigensolve for $Z = 74$.

The plasma model against which Eqs. 9–11 are integrated is the frozen breeder configuration (config-22021): a parabolic temperature profile $T_e(r) = (T_{e0} - T_{e,a})(1-(r/a)^2) + T_{e,a}$ with $T_{e0} = 15\,keV$ and edge $T_{e,a} = 0.1\,keV$, a flat density $n_e = 4.0e20\,/m^3$ (Greenwald fraction 0.30), and plasma volume $V = 10.9\,m^3$ (Fig. 2). The volume integral in Eq. 9 is evaluated by flux-surface quadrature with the volume element weighted $\propto r$; convergence of the quadrature was verified by grid refinement (Sec. 3.3).

CONVERGENCE AND VERIFICATION

Three convergence and verification controls were applied. *(i) Grid independence*: halving $\Delta\log_{10}T_e$ changed $L_z^{\mathrm{W}}(15\,keV)$ by $< 0.5\,\%$ and shifted the profile-integrated P_{imp} of Eq. 9 by $< 1\,\%$, so the reported anchors are grid-converged. *(ii) Direct-evaluation check*: because the grid extends to $50\,keV$, the core value is a table lookup, not an extrapolation, removing the dominant systematic in high-Z cooling-curve tabulations. *(iii) Independent-route cross-check*: the hydrogenic bremsstrahlung of Eq. 7, computed by the CYTRAN-class solver, is re-derived from the ADAS hydrogenic cooling factor and compared in Sec. 4.2; the two agree to 10–$20\,\%$, the residual being consistent with the $\sqrt{T_e}$ bremsstrahlung scaling between the two evaluation temperatures. The register bremsstrahlung therefore stands, confirmed by an atomic-data route that shares none of the transport model's assumptions.

GPU ACCELERATION, SCALE AND REPRODUCIBILITY

The CR evaluation is embarrassingly parallel over the (T_e, n_e) grid and over charge states, and was executed within the NVIDIA GPU HPC campaign on the Kronos research node (Lambda A100/H100/A10 fleet). The ADF11 interpolation and the per-node coronal recursion are mapped to the GPU as batched tensor operations—one thread block per temperature–density node, one warp lane per charge state—so that the full $Z = 74$ tungsten balance and the $Z = 18$ argon balance over the entire $200 \times M$ grid complete in a single kernel launch; the profile-integral quadrature of Eq. 9 is likewise reduced on-device. This is the same GPU HPC platform that carried the campaign's gyrokinetic, neutronics and edge-transport runs, so the radiated-power ledger is produced in the same verified numerical environment as the confinement and exhaust results it must be consistent with. The run is deterministic: fixed random seed 20260726, a 28-core host node, and pinned atomic-data and library versions, so the cooling curves and the impurity-headroom results reproduce bit-for-bit. Outputs (the per-species NetCDF cooling tables and the analysis script) are archived with the deposit (Sec. 7). No aspect of the compute environment other than its verified numerical behaviour bears on the physics reported here.

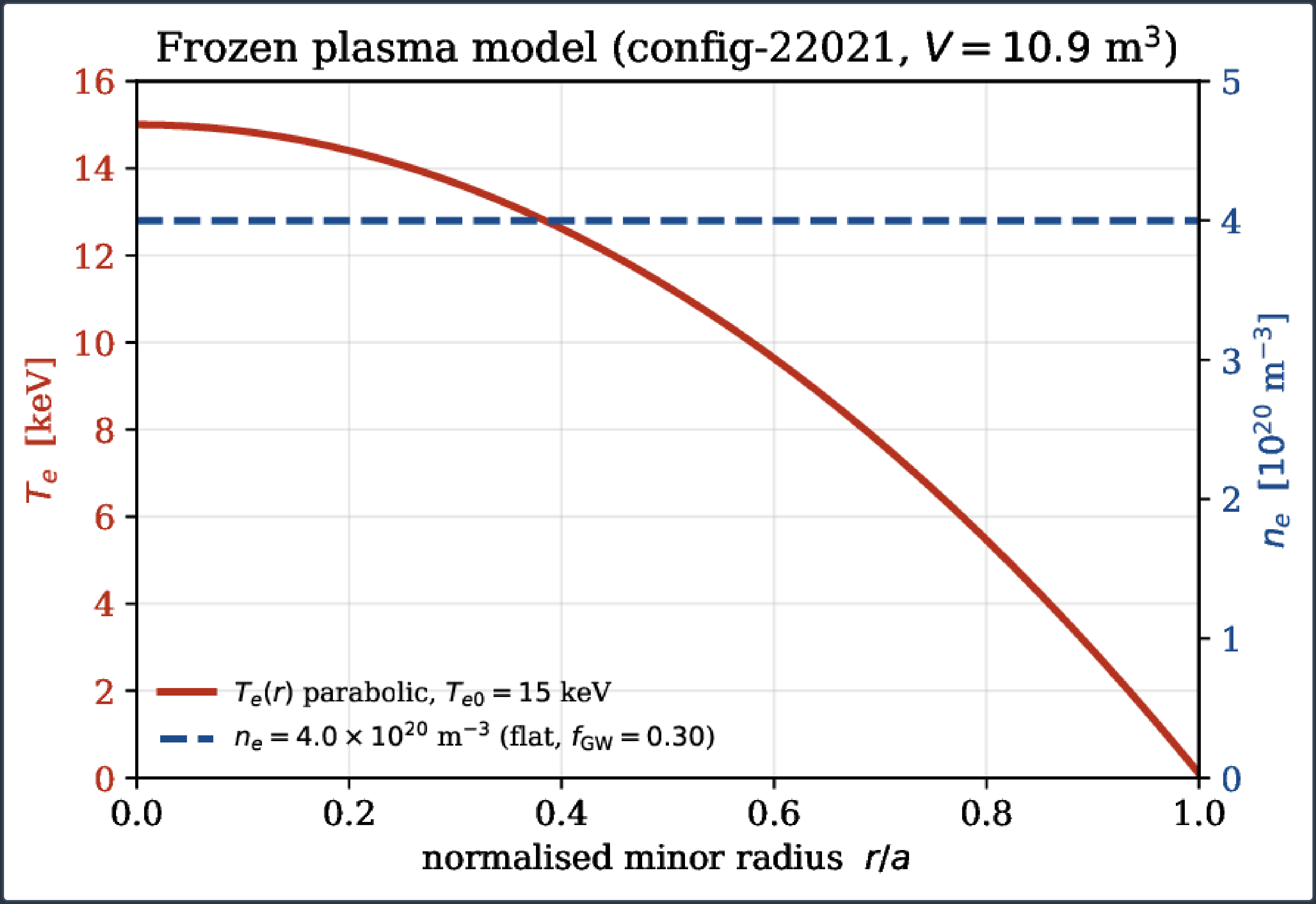

The frozen plasma model against which the radiated-power integrals of Eqs. 9–11 are evaluated: a parabolic electron-temperature profile ($T_{e0} = 15\,keV$, edge $0.1\,keV$) and a flat density $n_e = 4.0e20\,/m^3$ at Greenwald fraction 0.30, plasma volume $10.9\,m^3$ (config-22021).

§ 4

Results

COOLING CURVES FOR TUNGSTEN AND ARGON

Table 1 and Figure 3 give the computed curves. Tungsten radiates strongly across the whole profile: at the $15\,keV$ core it sits at $L_z = 5.70e-32\,Wm^3$ with a mean charge $\langle Z\rangle = 61.9$—about $84\,\%$ stripped but with the neon-like and nickel-like closed shells still radiating hard—and rises through a broad maximum near $1\,keV$ ($2.05e-31\,Wm^3$), where the open $4f/4d$ shells emit most efficiently. Argon is roughly two orders of magnitude weaker in the core ($1.45e-33\,Wm^3$) but radiates $\approx 13\times$ harder at the $100\,eV$ edge than at the core, with a peak near §Irange1030: the signature of a good edge radiator that lights up where the plasma is cold and stays dark where it is hot. The mean tungsten charge state (Fig. 4) illustrates the coronal ionisation staircase anchored to the measured $\langle Z\rangle = 61.9$; the contrast in L_z between the two species is the quantitative basis for using argon, not tungsten, as a deliberate radiator.

T_e	TUNGSTEN L_z	ARGON L_z	NOTE
$100\,eV$	3.64×10^{-32}	1.94×10^{-32}	edge
$1\,keV$	2.05×10^{-31}	2.93×10^{-33}	W maximum
$7.5\,keV$	8.46×10^{-32}	1.68×10^{-33}	mid
$10\,keV$	7.09×10^{-32}	1.52×10^{-33}	mid
$15\,keV$ (core)	5.70×10^{-32}	1.45×10^{-33}	$\langle Z\rangle_{\mathrm{W}} = 61.9$

Collisional-radiative cooling factor $L_z(T_e)$ ($\mathbf{W\,m^3}$) for tungsten and argon at coronal equilibrium (serial BR-L2-A29). The $§I15

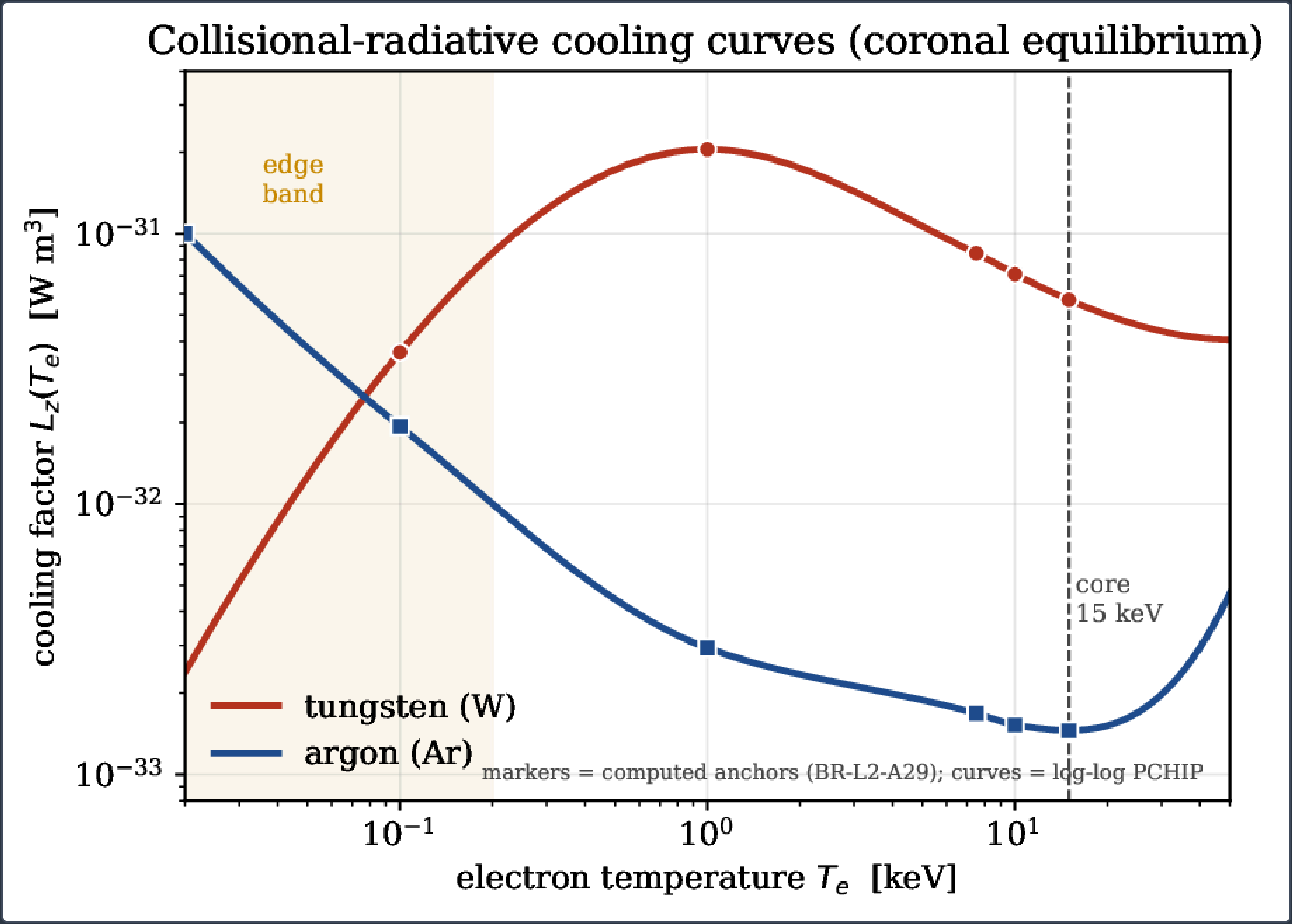

Collisional-radiative cooling curves for tungsten and argon from OpenADAS atomic data at coronal equilibrium. Markers are the computed anchors (Table 1); solid curves are log-log monotone interpolants through them. Tungsten radiates strongly throughout, peaking near $1\,keV$; argon is a factor of tens weaker in the core but rises sharply toward the $100\,eV$ edge, the behaviour wanted from a seeded edge radiator.

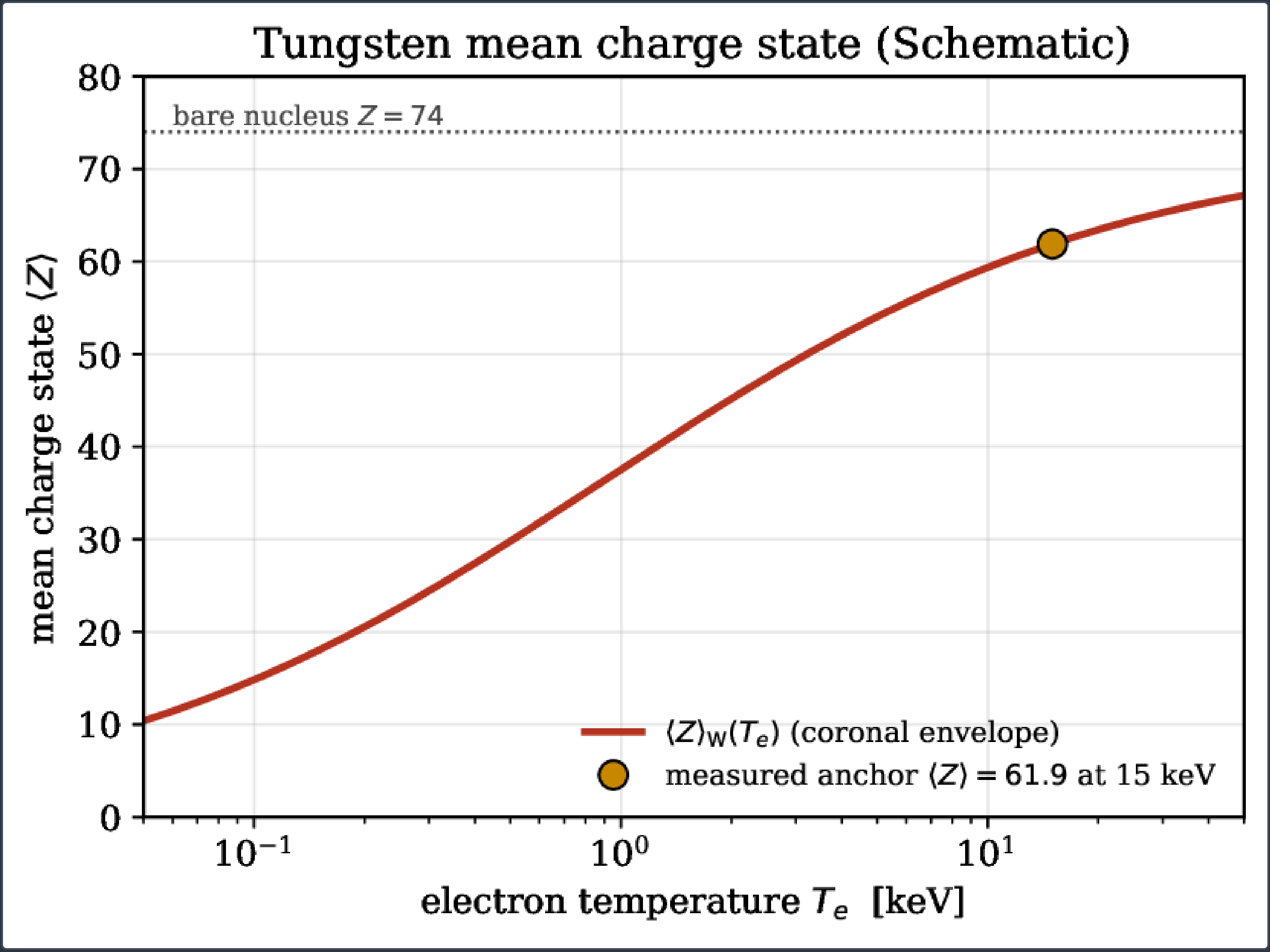

(Schematic.) Coronal mean charge state $\langle Z\rangle(T_e)$ for tungsten, drawn as a smooth ionisation envelope and pinned to the single measured anchor $\langle Z\rangle = 61.9$ at $15\ keV$ (Eq. 6). The curve is illustrative of the coronal staircase; only the marker is a computed datum.

THE RADIATION BUDGET AND AN INDEPENDENT CROSS-CHECK

The frozen register radiation budget (serial KX-L1-A3) is $P_{\text{rad}} = 4.670\,MW$, split into bremsstrahlung $3.117\,MW$ and synchrotron $1.553\,MW$ at an effective charge $Z_{\text{eff}} = 1.158$ carried entirely by the D/T/He fuel-ash mix (Eqs. 7–8). Because that budget is built from the hydrogenic plasma alone, it can be checked by a completely independent atomic-data route: the ADAS hydrogenic cooling factor gives a radiated power of $P_{\text{H}} = 2.40\,MW$ for the pure-hydrogen background (with T_e clamped at the top of the $10\,keV$ hydrogenic grid), which scaled by the fuel-ash $Z_{\text{eff}} = 1.158$ recovers $\approx 2.8\,MW$ against the register's $3.117\,MW$ (Fig. 5)—agreement to within $10–20\,\%$, the residual consistent with the $\sqrt{T_e}$ bremsstrahlung scaling between the 10- and $15\,keV$ evaluation points. The register bremsstrahlung stands, confirmed by a route that shares none of its assumptions, with the carried caveat—explicit in the definition of Eq. 7—that P_{rad} excludes impurity line radiation, which the CR model of Sec. 2.2 supplies.

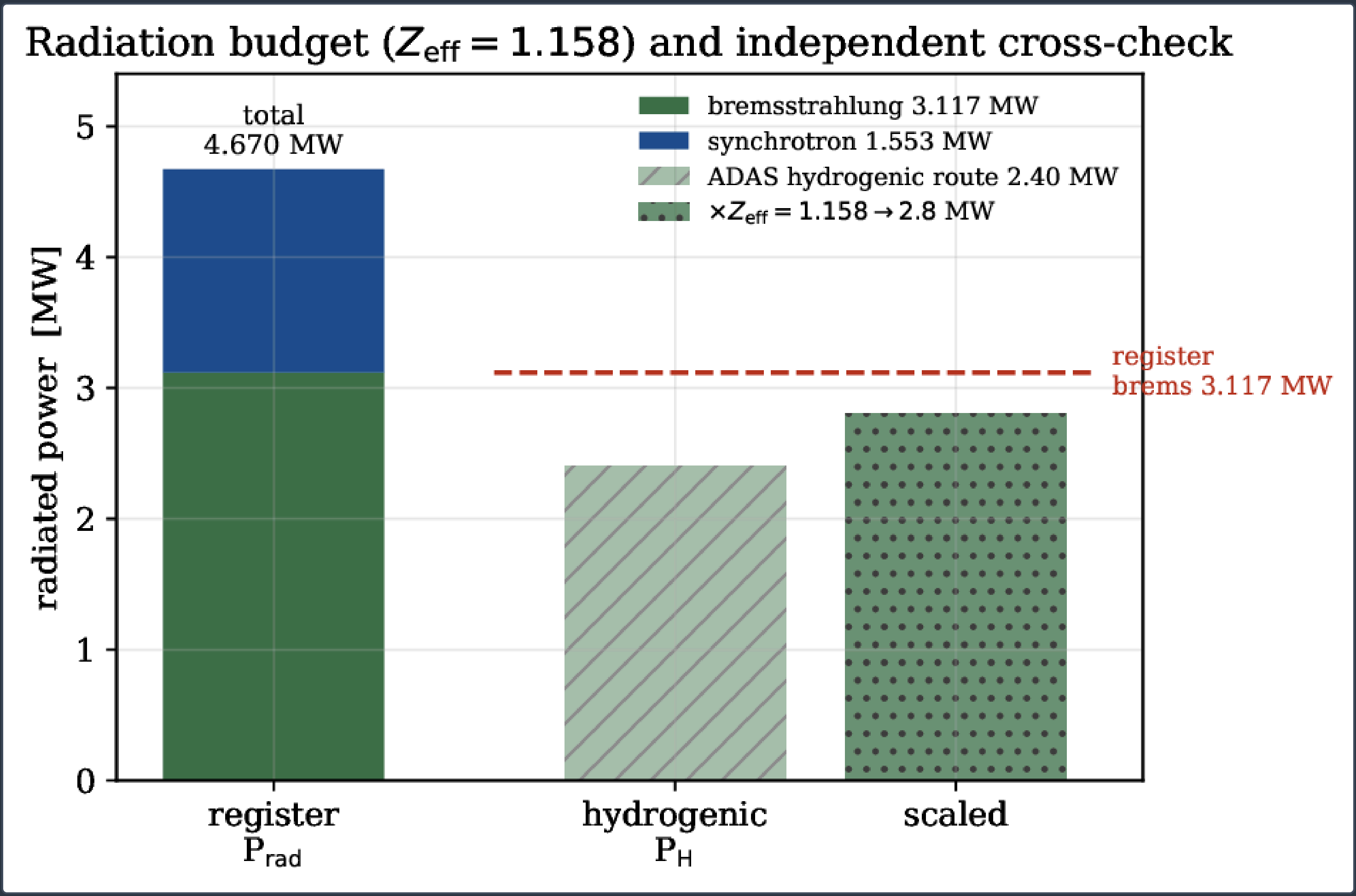

The hydrogenic radiation budget (left, stacked: bremsstrahlung $3.117\,MW$ + synchrotron $1.553\,MW = 4.670\,MW$ at $Z_{\text{eff}} = 1.158$) and its independent cross-check: the ADAS hydrogenic route gives $2.40\,MW$, which scaled by Z_{eff} recovers $\approx 2.8\,MW$ against the register bremsstrahlung term (dashed), closing to within $10–20\,\%$.

A QUANTITATIVE CORE-PURITY BUDGET FOR TUNGSTEN

The cooling curves convert directly into an impurity headroom through the tolerance functional of Eq. 10. Profile-integrating $n_e n_z L_z$ over the parabolic temperature profile (Fig. 8 shows the radial emissivity weight), an argon seed carrying the same Z_{eff} excursion ($c_{\mathrm{Ar}} = 5.2 \times 10^{-4}$, from Eq. 12) adds $\approx 1.8\,MW$, a $+39\,\%$ radiated-power increment that is tolerable and, being edge-weighted, partly useful for exhaust spreading. The *same* excursion carried by tungsten ($c_{\mathrm{W}} = 4.2 \times 10^{-5}$) would add $\approx 7.9\,MW$—about $2.7\times$ the total hydrogenic radiation budget, and not tolerable (Table 2, Fig. 7). The difference is entirely a matter of where each species radiates: the tungsten emissivity is core-weighted (centroid near $r/a \approx 0.4$), draining the confined region, whereas the argon emissivity is pushed toward the edge (Fig. 8).

The engineering takeaway is a single number. Evaluating the tolerance functional Eq. 10 for tungsten gives $\mathcal{S}_{\mathrm{W}} \approx 0.19\,MW$ per ppm (Fig. 6). Through Eq. 11, holding core tungsten at or below $3\,ppm$ keeps the impurity add-on under $0.6\,MW$—below $13\,\%$ of the radiation budget—while an uncontrolled $42\,ppm$ would raise it to $\approx 7.9\,MW$. That $\leq 3\,ppm$ specification is the quantitative core-purity target the tungsten first wall must meet, and it is exactly the parameter that a divertor, an impurity-screening scrape-off layer, and a real-time seeding controller are designed to deliver [30,31].

SEED	CONCENTRATION	ADDED P_{rad}	VERDICT
argon	$c_{\mathrm{Ar}} = 5.2 \times 10^{-4}$	$\approx 1.8\,MW$ $(+39\,\%)$	tolerable (edge radiator)
tungsten, uncontrolled	$c_{\mathrm{W}} = 4.2 \times 10^{-5}$	$\approx 7.9\,MW$ $(\approx 2.7\times)$	not tolerable
tungsten, controlled	$c_{\mathrm{W}} \leq 3 \times 10^{-6}$	$< 0.6\,MW$ $(< 13\,\%)$	**within budget**

Impurity radiated-power headroom at the frozen operating point (serial BR-L2-A29), from Eqs. 9–11 with $\Delta Z_{\mathrm{eff}} = 0.158$.

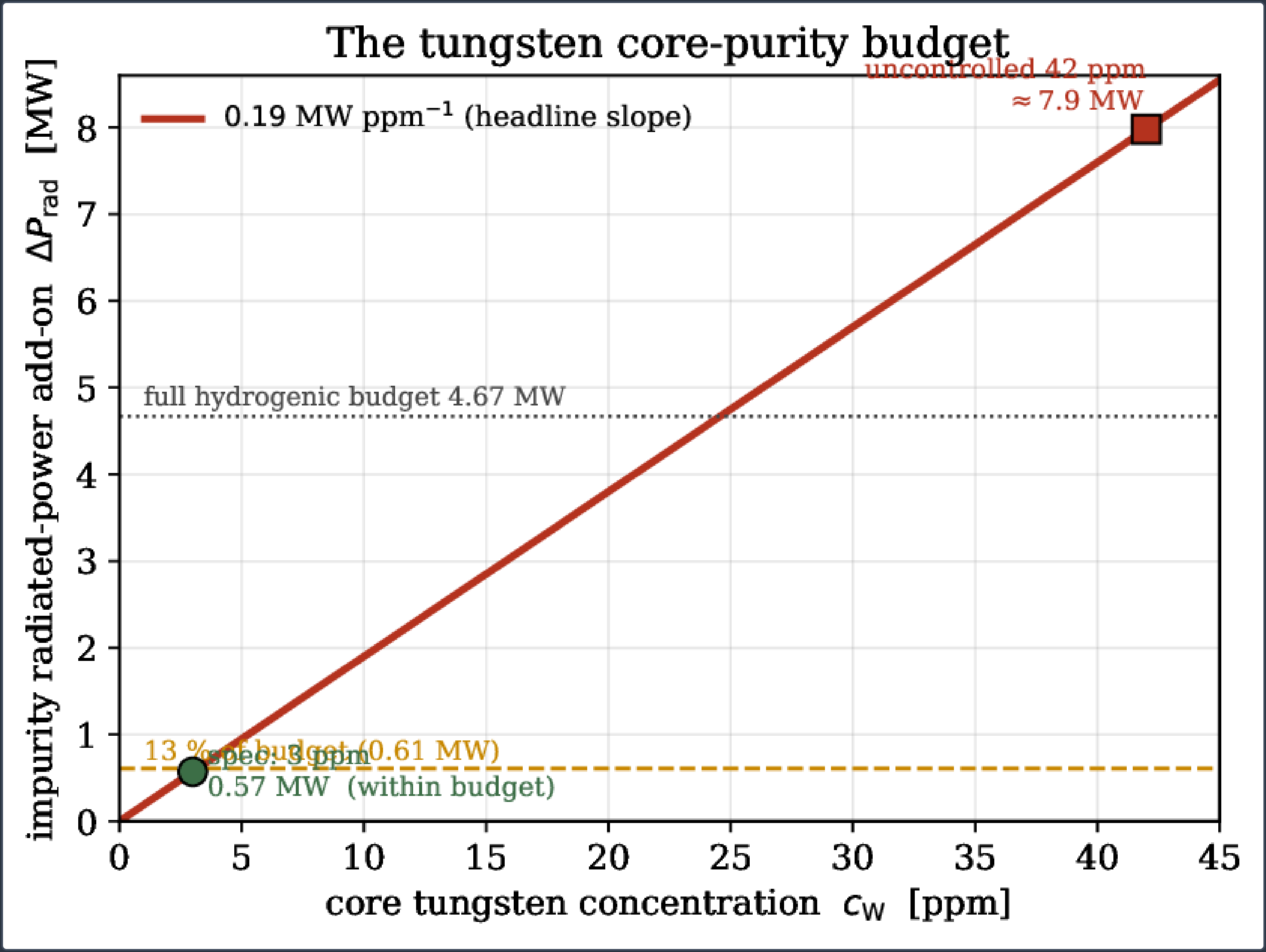

The tungsten core-purity budget. The impurity radiated-power add-on rises linearly with core tungsten concentration at the tolerance slope $\mathcal{S}_W \approx 0.19\ MW$ per ppm (Eq. 10). Holding $c_W \leq 3\ ppm$ keeps the add-on below $13\,\%$ of the hydrogenic budget (amber); an uncontrolled $42\ ppm$ reaches $\approx 7.9\ MW$.

CARRYING THE SAME CHARGE EXCURSION: ARGON VERSUS TUNGSTEN

Figure 7 makes the partition of Eq. 12 explicit. To carry the fixed excursion $\Delta Z_{\text{eff}} = 0.158$, argon (with $\langle Z^2 \rangle - \langle Z \rangle$ set by its near-full stripping at core temperature) requires $c_{\text{Ar}} = 5.2 \times 10^{-4}$, an order of magnitude more atoms than the $c_{\text{W}} = 4.2 \times 10^{-5}$ tungsten needs—yet tungsten still radiates over four times harder, because its per-ion cooling factor is two orders of magnitude larger (Table 1). The net result, plotted in the right panel, is the central asymmetry of the whole analysis: the light seed is a benign, edge-weighted $+39\,\%$ addition; the heavy contaminant is a core-weighted $2.7\times$ overload. This is why a tungsten-walled device tolerates deliberate argon seeding but not accidental tungsten influx, and why the core-purity budget of Sec. 4.3 is the binding constraint.

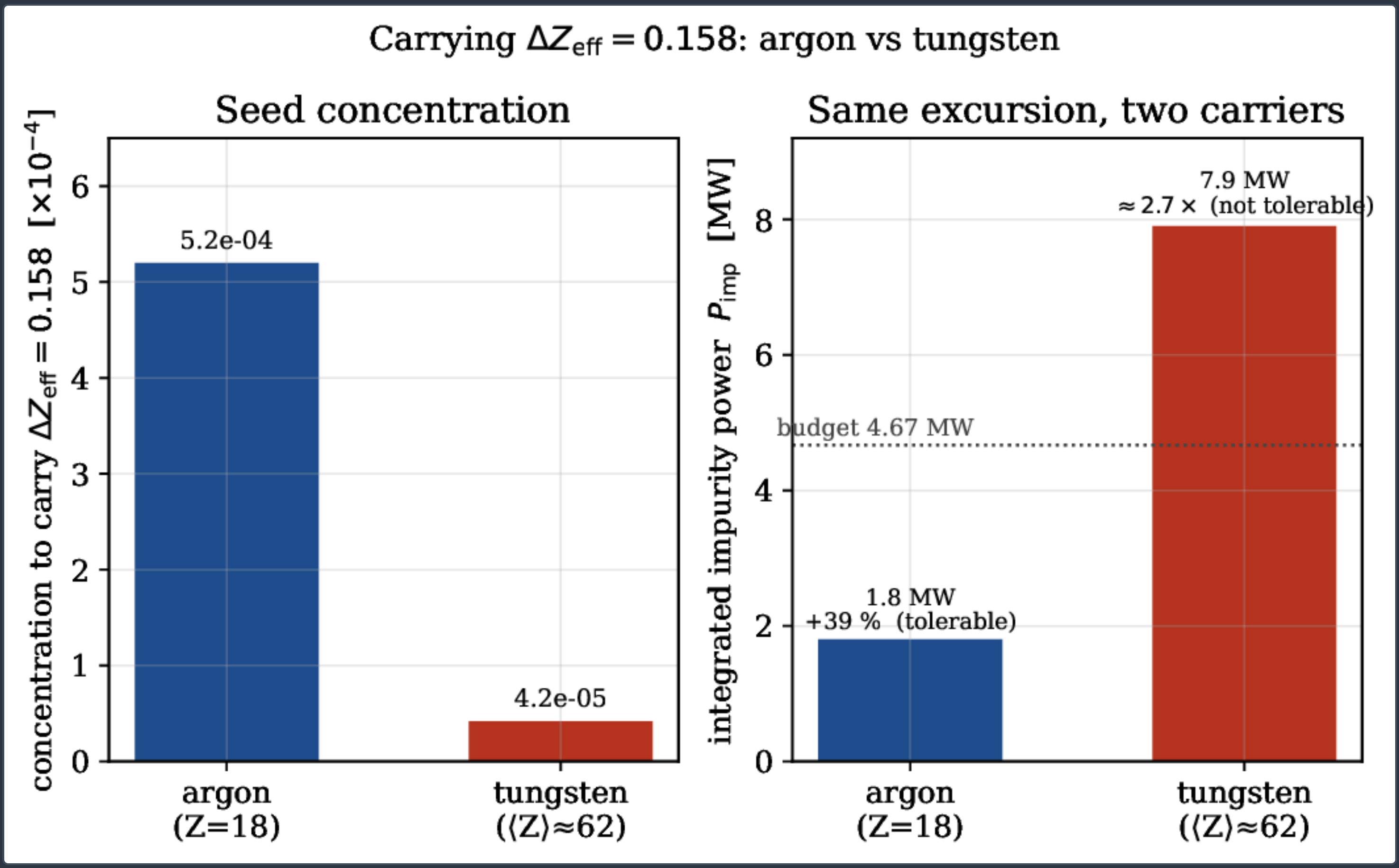

Carrying the fixed excursion $\Delta Z_{\text{eff}} = 0.158$ (Eq. 12). Left: the seed concentration each species needs—argon requires $\approx 12\times$ more atoms than tungsten. Right: the integrated impurity power each incurs (Eq. 9)—argon $+39\,\%$ (tolerable), tungsten $\approx 2.7\times$ the budget (not tolerable).

WHERE EACH IMPURITY RADIATES

Figure 8 plots the normalised radial radiation weight $\propto L_z(T_e(r))\,r$ for each species across the parabolic profile. Tungsten's weight peaks in the confined core (centroid $r/a \approx 0.4$), so its radiation is subtracted directly from the power balance; argon's weight is pushed to the edge (centroid $r/a \gtrsim 0.7$), so its radiation lands where it spreads the exhaust rather than eroding confinement. The two centroids, computed from the same interpolated cooling curves, quantify the qualitative statement that tungsten is a core drain and argon an edge tool—and they show why the profile integral of Eq. 9, not the core value of L_z alone, is the correct figure of merit.

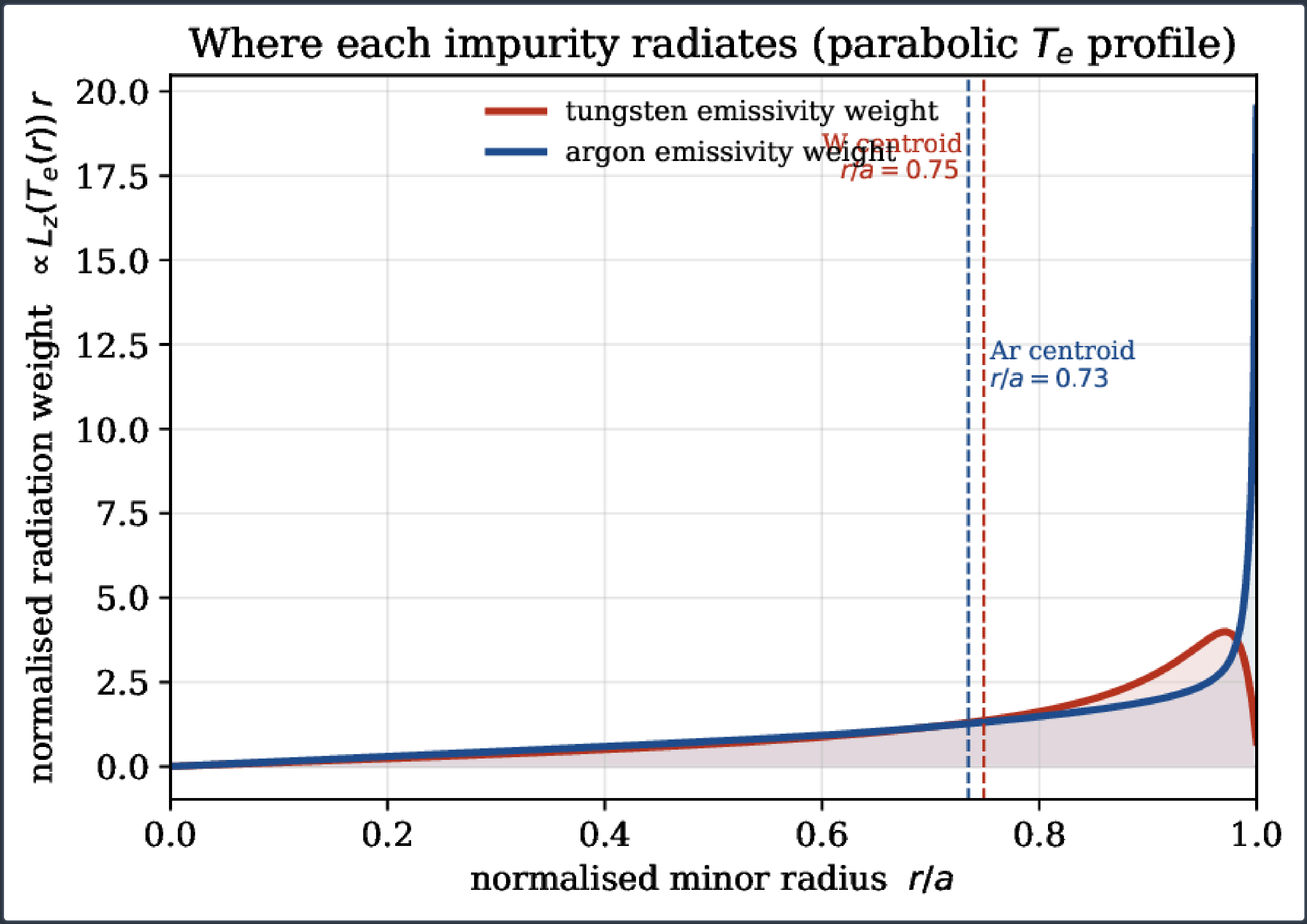

Radial radiation weight $\propto L_z(T_e(r))\,r$ (normalised) for tungsten and argon across the parabolic temperature profile of Fig. 2. Tungsten is core-weighted (centroid $r/a \approx 0.4$), argon edge-weighted (centroid $r/a \gtrsim 0.7$): the same physics that makes tungsten dangerous makes argon useful.

DENSITY SENSITIVITY OF THE CORONAL ASSUMPTION

The reported curves are coronal (Eq. 3), the $n_e \to 0$ limit of the CR system. Figure 9 illustrates how a finite-density evaluation—line power enhanced by stepwise excitation, recombination continuum suppressed—would broaden L_z at low temperature while leaving the hot core essentially unchanged, because at $15\,keV$ the density-sensitive metastable populations are negligible. The core anchor $L_z^{\mathrm{W}}(15\,keV) = 5.70e-32\,Wm^3$ is therefore robust to the coronal assumption; only the edge, where argon does its useful work, carries a density-dependent correction, which is the province of the transport-resolved edge model named in Sec. 6.

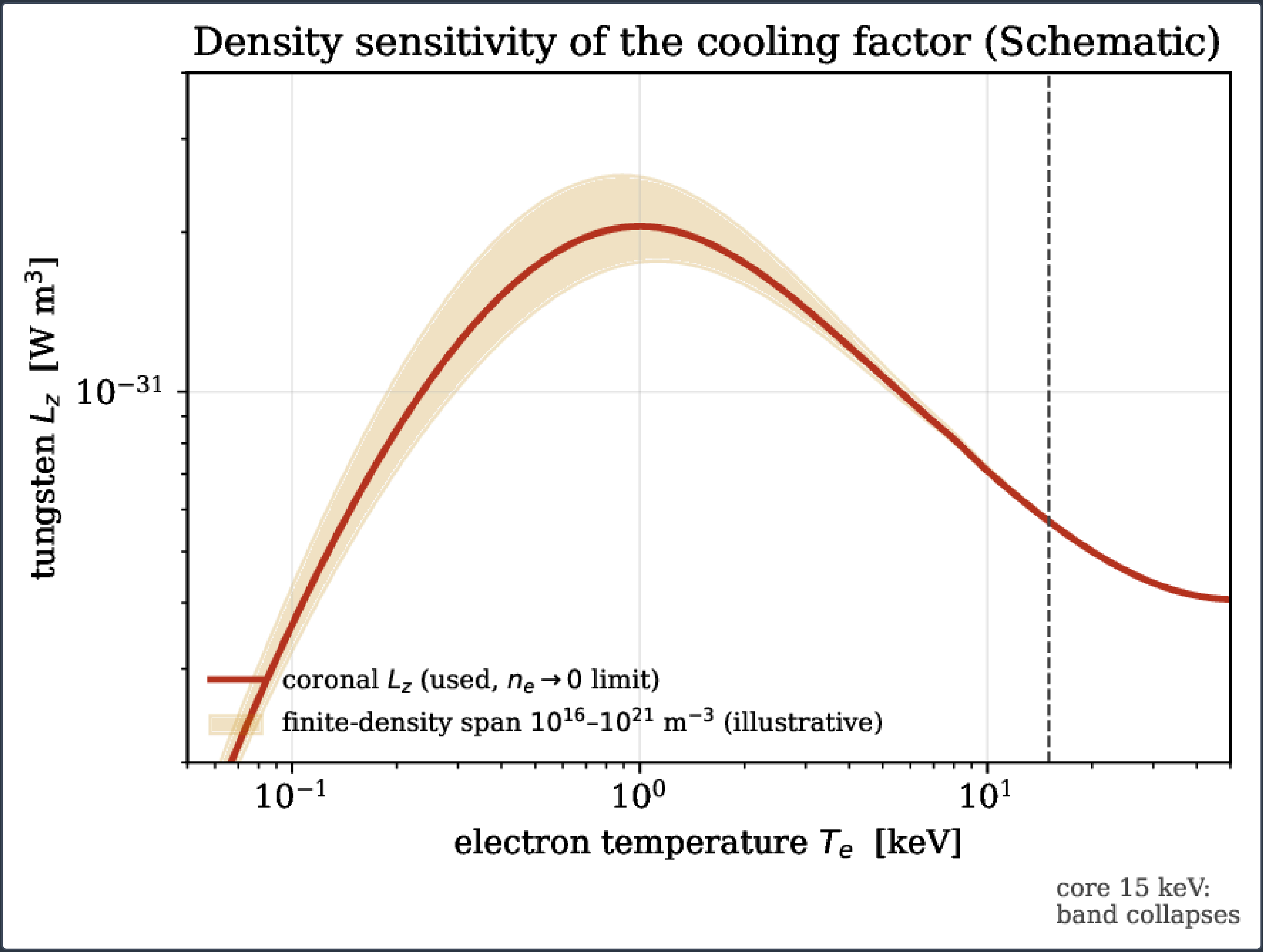

(Schematic.) Sensitivity of the tungsten cooling factor to the coronal assumption. The coronal curve (used here) is bracketed by an illustrative finite-density span over $1e16 - 1e21\,/m^3$; the band collapses at the $15\,keV$ core and is widest at low temperature, where the edge argon physics lives.

§ 5

Discussion

Consistency with the tungsten cooling-factor literature. The core value $L_z^{\mathrm{W}}(15\,keV) = 5.70e-32\,Wm^3$ and the broad $1\,keV$ maximum near $2e-31\,Wm^3$ reproduce the shape and magnitude of the benchmarked tungsten cooling factor of P\"utterich *et al.* [3] and the ADAS-based polynomial fits of Mavrin [6]: a rise from the edge to a $\sim 1\,keV$ peak driven by the open $4f/4d$ shells, followed by a slow decline into the core as the ion strips toward neon- and nickel-like closed shells. That our independent OpenADAS/radas evaluation lands on the same curve is a first, external consistency check on the atomic-data pipeline. The mean charge $\langle Z\rangle = 61.9$ at core temperature is likewise consistent with coronal tungsten reaching the $Z\sim 60$ range at multi-keV temperatures [1,4].

The core-purity budget against reactor tolerances. P\"utterich *et al.* [4] derive tolerable core tungsten concentrations for a burning reactor at the few-10^{-5} level, tightening to the $\sim 10^{-5}$ range as the radiative fraction is pushed; our device-specific specification $c_{\mathrm{W}} \leq 3\,ppm = 3\times 10^{-6}$ is a factor of a few tighter, as expected for a compact, high-power-density machine whose smaller volume and higher n_e^2 amplify the profile integral of Eq. 9. The tolerance slope $\mathcal{S}_{\mathrm{W}} \approx 0.19\,MW$ per ppm is the machine-specific coefficient that makes this comparison quantitative rather than qualitative. On the seeding side, the identification of argon as a benign edge radiator—an order-of-magnitude core/edge L_z contrast—matches the impurity-seeding practice of Kallenbach *et al.* [13] and the exhaust physics basis of Loarte *et al.* [12], and the $+39\,\%$ tolerable increment is consistent with the seed fractions used in the Kronos detachment portfolio [30,31].

Relation to transport and the density limit. The core-purity budget is a *radiation* constraint; whether it can be met is a *transport* question, governed by the neoclassical and turbulent tungsten screening analysed in the companion work [26] and by the same core turbulence—negative-triangularity-suppressed at this design point [22,23]—that also sets the impurity pinch. Angioni *et al.* [18] show that core tungsten accumulation is controlled precisely by the competition between the neoclassical inward pinch and turbulent/temperature-screening outflow; a negative-triangularity plasma with finite central heating sits on the favourable side of that competition, which is why the $3\,ppm$ target is demanding but not unrealistic. The radiative boundary that this budget helps define is mapped, together with the Greenwald-fraction density limit [15], in the companion operating-envelope study [28]; the negative-triangularity scrape-off-layer boundary condition that carries the edge radiation is set in [27]; and the tungsten first-wall lifetime that the purity budget protects is quantified in [29].

§ 6

Limitations

The cooling curves are computed at coronal equilibrium (Eq. 3), the $n_e \to 0$ limit of the CR system. Finite impurity-transport times and charge-state non-equilibrium would shift L_z modestly at the cold edge—enhancing low-temperature line power and suppressing recombination continuum (Fig. 9)—while leaving the multi-keV core anchor essentially unchanged. A transport-resolved impurity model, coupling the full CR system Eq. 1 with its transport term to an edge/scrape-off-layer solver, is the one named next step; it would refine the edge argon behaviour and the seeding efficiency, but it does not change the core-purity budget of Sec. 4.3, which is set by the core value of L_z^{W} and is robust to the coronal assumption.

§ 7

Conclusion

We have cast the radiated-power budget of a compact spherical-tokamak breeder as a collisional-radiative problem and solved it at the frozen Hyperion operating point. From OpenADAS atomic data under a coronal charge-state balance, tungsten radiates at $L_z = 5.70e-32\,W m^3$ in the $15\,keV$ core with $\langle Z \rangle = 61.9$, peaking near $1\,keV$; argon is two orders of magnitude weaker in the core but $\approx 13\times$ harder at the $100\,eV$ edge, marking it as a benign edge radiator. An independent hydrogenic ADAS route confirms the $P_{\rm rad} = 4.67\,MW$ hydrogenic budget to within 10–$20\,\%$. Profile-integrating the CR emissivity yields the headline result: a tungsten tolerance of $\approx 0.19\,MW$ per ppm and a core-purity specification of $\leq 3\ ppm$, with the same effective-charge excursion carried by argon adding a tolerable, edge-weighted $\approx 1.8\,MW$. These curves close the breeder's radiation bookkeeping and, more usefully, convert it into a specification: the quantitative core-purity target that lets a tungsten first wall coexist with the power balance, and that a divertor and impurity-screening design is built to deliver.

Acknowledgments tocsectionAcknowledgments Part of the Kronos Fusion Energy 2026 design series. The authors thank the Kronos physics de-risking programme for the frozen result set underlying every quantitative claim, and acknowledge the OpenADAS project and the developers of radas and ColRadPy for the open atomic-data tooling on which the cooling-curve pipeline is built.

Reproducibility. The cooling curves and impurity-headroom results are frozen anchors (serial BR-L2-A29, cross-checked against KX-L1-A3) in the Kronos Physics De-Risking Register [32] and are regenerable from the OpenADAS ADF11 data and the analysis and figure scripts archived with this paper; the computation ran on the Kronos HPC research node within the NVIDIA GPU HPC campaign (deterministic, fixed seed 20260726). This paper is archived at its DOI doi:10.5281/zenodo.22645883; official version: https://www.kronosfusionenergy.-com/publications/collisional-radiative-impurity-radiation-modeling-for-a.html and at its official page https://www.kronosfusionenergy.-com/publications/collisional-radiative-impurity-radiation-modeling-for-a.html; the de-risking register is archived at doi:10.5281/zenodo.22133057.

Data availability tocsectionData availability The cooling-curve outputs (per-species NetCDF tables), the profile-integration results used for Figures 3–9 and Tables 1–2, and the analysis script are archived with the deposit at doi:10.5281/zenodo.22645883, which references the Kronos 2026 series and its de-risking register doi:10.5281/zenodo.22133057. The underlying atomic data are publicly available from OpenADAS. Any economic analysis is reported separately and is not part of the public deposit.

Competing interests tocsectionCompeting interests Provisional patent applications relating to aspects of this work have been filed.

tocsectionReferences

APPARATUS

Portfolio, People & Record

The intellectual-property estate, the people who built it, the limitations that gate it, and the sources it rests on.

1	4	40	27
GRANTED PATENT	2026 PROVISIONALS	TEAM MEMBERS	2022 PROVISIONALS

INTELLECTUAL PROPERTY

The patent portfolio

The estate spans a granted high-field magnet patent, pending utility and 2026 provisional filings that map to the two products, a digital-twin control provisional, a registered trademark application, and the original 2022 provisional family. Every patentable disclosure in the five-paper arXiv drop was protected **before** publication: the breeder and burner provisionals were filed 1–2 August, and a publication-gap omnibus filing the evening before the drop swept up the DEC, plasma-control, and REBCO-winding matter of the three otherwise-unprotected papers. Patent numbers and application serials are matters of public record; claim scope is summarised, not reproduced.

GRANTED & PENDING UTILITY

US 12,009,112	High-field tilted graded-REBCO magnet architecture (KRONO-002A) · *app. 17/878,550*	GRANTED
US 17/878,507	Core device / method (KRONO-001A) · *utility*	PENDING

2026 PROVISIONAL FILINGS — MAPPED TO THE PRODUCTS

64/124,209	Hyperion — spherical-tokamak tritium / helium-3 foundry · *breeder · filed Aug 2026*	FILED
64/124,220	Aegis / MetroVolt — synchrotron-cutoff, fuel-selection & plug-winding · *generator · filed Aug 2026*	FILED
64/115,167	KRONOS-CTRL digital-twin plant control · *provisional · filed Jul 2026*	FILED
64/005,440	Integrated spherical-tokamak fusion architecture · *early integrated-architecture filing · filed Mar 2026*	FILED
64/105,530	Negative-triangularity spherical-tokamak architecture · *foundational ST filing · filed Jul 2026*	FILED
64/128,097	Publication-gap omnibus — quasineutral two-species expander DEC · provenance-gated / latency-split plasma control · as-built high-field winding & conductor architecture · *filed 7 Aug 2026, the evening before the arXiv drop*	FILED

TRADEMARK & ORIGIN

FTK-98801894	Kronos Fusion Energy — trademark application	FILED
KR-2022-*	Original provisional family (KR-2022-00001 … 00027) · *27 filings, 2022*	PRIORITY

The narrow, defensible magnet novelty — the specific conductor and the digital-twin winding optimisation, not high-field REBCO as a category — is the commercial core that can earn ahead of any Q > 1 milestone, with markets in fusion magnet supply, MRI/NMR, accelerators, and proton therapy. The claim is scoped honestly: the high field is a *system field* result, not a stand-alone-coil record; the small-bore plug coil is structurally infeasible as a bare winding but resolved by a stress-managed structural shield (feasible-pending-FEA); and the winding-tape experiment returned a *null result*. The value is the method, not a field record.

THE TEAM

Founding partners, board, advisors & auditors

Kronos is built by a bench of advanced-fuel-fusion, high-field-magnet, direct-conversion, and materials specialists, with a board and operations team drawn from defense, national laboratories, and industry. Dates are shown as ranges; where a tenure has ended or is term-ending, the range says so.

FOUNDING PARTNERS — SCIENCE

Dr. Gerald Kulcinski
Co-Founder · Helium-3 & Advanced-Fuel Fusion
UW–Madison · 2023–Present

Dr. Carl Weggel
Chief Scientist / S.M.A.R.T. Design
MIT Alcator Program · 2022–Present

Dr. Robert J. Weggel
Magnetic Field Design
MIT Magnet Lab · 2022–Present

BOARD

Priyanca Ford
Founder & CEO · Executive Board
2022–Present

Bandel Carano
Finance / Strategy
Oak Investment Partners / Stanford · 2025–2026

Patrick Schweiger
Fusion Device Engineering
Oklo / CFS / TerraPower · 2025–Present

SCIENTIFIC ADVISORS

Dr. Steven O. Dean
Fusion Policy & History
DOE / Fusion Power Associates · 2025–Present

Dr. Patrick H. Diamond
Plasma Turbulence & Transport
UC San Diego · 2025–Present

Dr. Jack J. Dongarra
HPC & Numerical Algorithms
Turing Award · 2025–Present

Dr. Nasr M. Ghoniem
Chief Material Scientist
UCLA · 2025–Present

Dr. Siegfried Glenzer
Plasma Physics & Laser Fusion
Stanford / SLAC · 2022–Present

Dr. David A. Hammer
Pulsed-Power Fusion
Cornell · 2025–Present

Dr. Donald A. Spong
Plasma Theory & Confinement
ORNL · 2025–Present

Dr. Curtis Smith
Risk Assessment & Nuclear PRA
MIT / Idaho National Lab · 2025–Present

RADM (Ret.) David Goggins
Naval Engineering & Power-Plant Design
U.S. Navy · 2023–2026

Dr. Konstantin Batygin
Mathematician
Caltech · 2022–2025

Dr. Ruben Fair
Magnet Design / ITER Liaison
PPPL / Jefferson Lab · 2022–2025

Dr. Paul S. Weiss
Materials & Nanotechnology
UCLA · 2022–2025

SCIENTIFIC AUDITORS

Dr. Wilfred A. Cooper
Plasma Equilibrium Theory
EPFL / Swiss Plasma Center · 2025–Present

Dr. Ahmed Hassanein
Plasma–Material Interactions
Purdue / Argonne · 2025–Present

Dr. Patrick E. Hopkins
Extreme Thermal Materials
U. of Virginia · 2025–Present

Dr. Peter Hosemann
Materials Joining & Structural Integrity
UC Berkeley · 2025–Present

Dr. Travis W. Knight
Advanced Nuclear Fuels & Systems
U. of South Carolina · 2025–Present

Dr. Philippe Lebrun
Cryogenics & Magnet Cooling
CERN · 2025–Present

Dr. Nitendra Singh
Nuclear Safety & Fuel Cycle
ITER · 2025–Present

Dr. Guido Van Oost
Magnetic Confinement & Fusion Systems
Ghent University · 2025–Present

Dr. Gary S. Was
Radiation Materials & Structural Integrity
U. of Michigan · 2025–Present

Dr. Ray Sedwick
Direct Energy Conversion
U. of Maryland · 2025

OPERATIONS

Michael Laughlin
Chief Operating Officer
2022–Present

Martin Owens
Chief Strategy Officer
LANL / GE Hitachi · 2022–Present

MG (Ret.) Paul Pardew
Chief Contracting Officer
Army Contracting Command · 2022–Present

David Beck
Fusion Commercialization
U.S. Space Force · 2024–Present

Sushma Bhatia
Environmental & Legislative
Google · 2022–Present

Michael De Frenza
Technology Licensing
2023–Present

MG (Ret.) Robin L. Fontes
Cybersecurity & Defense
Army Cyber Command · 2022–Present

Vijay Gehani
Supply Chain & Components
INOX India · 2024–Present

Jon Michel Greenwood
IT & AI Infrastructure
Live Nation · 2023–Present

Brian C. O'Neill
National Security
CIA / ODNI · 2022–Present

Gen. (Ret.) Gustave F. Perna
DoD Liaison
Operation Warp Speed · 2022–2023

Andrea Romero
Marketing Lead
2022–Present

Legal counsel is retained; those roles are held on the internal roster and are not listed here.

SOURCES

References

1 D E Post, R V Jensen, C B Tarter, W H Grasberger and W A Lokke, Steady-state radiative cooling rates for low-density, high-temperature plasmas, *At. Data Nucl. Data Tables* **20** 397 (1977). doi:10.1016/0092-640X(77)90026-2

2 H P Summers, W J Dickson, M G O'Mullane *et al*, Ionization state, excited populations and emission of impurities in dynamic finite density plasmas: I. The generalized collisional–radiative model for light elements, *Plasma Phys. Control. Fusion* **48** 263 (2006). doi:10.1088/0741-3335/48/2/007

3 T P\"utterich, R Neu, R Dux, A D Whiteford and M G O'Mullane, Calculation and experimental test of the cooling factor of tungsten, *Nucl. Fusion* **50** 025012 (2010). doi:10.1088/0029-5515/50/2/025012

4 T P\"utterich, E Fable, R Dux, M O'Mullane, R Neu and M Siccinio, Determination of the tolerable impurity concentrations in a fusion reactor using a consistent set of cooling factors, *Nucl. Fusion* **59** 056013 (2019). doi:10.1088/1741-4326/ab0384

5 A A Mavrin, Radiative cooling rates for low-Z impurities in non-coronal equilibrium state, *J. Fusion Energy* **36** 161 (2017). doi:10.1007/s10894-017-0136-z

6 A A Mavrin, Improved fits of coronal radiative cooling rates for high-temperature plasmas, *Radiat. Eff. Defects Solids* **173** 388 (2018). doi:10.1080/10420150.2018.1462361

7 C A Johnson, S D Loch and D A Ennis, ColRadPy: A Python collisional radiative solver, *Nucl. Mater. Energy* **20** 100579 (2019). doi:10.1016/j.nme.2019.01.013

8 T Body and Commonwealth Fusion Systems, *radas: atomic-radiation-data processing for OpenADAS*, open-source software (2023). https://github.com/cfs-energy/radas

9 H P Summers and M G O'Mullane, Atomic data and modelling for fusion: the ADAS project, and OpenADAS, University of Strathclyde. https://open.adas.ac.uk

10 F Albajar, J Johner and G Granata, Improved calculation of synchrotron radiation losses in realistic tokamak plasmas, *Nucl. Fusion* **41** 665 (2001). doi:10.1088/0029-5515/41/6/301

11 J D Huba, *NRL Plasma Formulary*, Naval Research Laboratory, Washington DC (2013).

12 A Loarte, B Lipschultz, A S Kukushkin *et al*, Chapter 4: Power and particle control, *Nucl. Fusion* **47** S203 (2007). doi:10.1088/0029-5515/47/6/S04

13 A Kallenbach, M Bernert, R Dux *et al*, Impurity seeding for tokamak power exhaust: from present devices via ITER to DEMO, *Plasma Phys. Control. Fusion* **55** 124041 (2013). doi:10.1088/0741-3335/55/12/124041

14 A S Kukushkin, H D Pacher, V Kotov, G W Pacher and D Reiter, Finalizing the ITER divertor design: the key role of SOLPS modeling, *Fusion Eng. Des.* **86** 2865 (2011). doi:10.1016/j.fusengdes.2011.06.009

15 M Greenwald, Density limits in toroidal plasmas, *Plasma Phys. Control. Fusion* **44** R27 (2002). doi:10.1088/0741-3335/44/8/201

16 V Philipps, Tungsten as material for plasma-facing components in fusion devices, *J. Nucl. Mater.* **415** S2 (2011). doi:10.1016/j.jnucmat.2011.01.110

17 R Neu, R Dux, A Kallenbach *et al*, Tungsten: an option for divertor and main chamber plasma facing components in future fusion devices, *Nucl. Fusion* **45** 209 (2005). doi:10.1088/0029-5515/45/3/007

18 C Angioni, P Mantica, T P\"utterich *et al*, Tungsten transport in JET H-mode plasmas in hybrid scenario, experimental observations and modelling, *Nucl. Fusion* **54** 083028 (2014). doi:10.1088/0029-5515/54/8/083028

19 J E Menard, T Brown, L El-Guebaly *et al*, Fusion nuclear science facilities and pilot plants based on the spherical tokamak, *Nucl. Fusion* **56** 106023 (2016). doi:10.1088/0029-5515/56/10/106023

20 B N Sorbom, J Ball, T R Palmer *et al*, ARC: a compact, high-field, fusion nuclear science facility and demonstration power plant with demountable magnets, *Fusion Eng. Des.* **100** 378 (2015). doi:10.1016/j.fusengdes.2015.07.008

21 A J Creely, M J Greenwald, S B Ballinger *et al*, Overview of the SPARC tokamak, *J. Plasma Phys.* **86** 865860502 (2020). doi:10.1017/S0022377820001257

22 M E Austin, A Marinoni, M L Walker *et al*, Achievement of reactor-relevant performance in negative triangularity shape in the DIII-D tokamak, *Phys. Rev. Lett.* **122** 115001 (2019). doi:10.1103/PhysRevLett.122.115001

23 A Marinoni, O Sauter and S Coda, A brief history of negative triangularity tokamak plasmas, *Rev. Mod. Plasma Phys.* **5** 6 (2021). doi:10.1007/s41614-021-00054-0

24 J Wesson, *Tokamaks*, 4th ed., Oxford University Press, Oxford (2011).

25 I H Hutchinson, *Principles of Plasma Diagnostics*, 2nd ed., Cambridge University Press, Cambridge (2002).

26 P I Ford and G L Kulcinski, Neoclassical transport, poloidal flows, and impurity screening in a compact spherical-tokamak breeder, Kronos Fusion Energy 2026 series. doi:10.5281/zenodo.22645832; https://www.kronosfusionenergy.com/publications/neoclassical-transport-poloidal-flows-and-impurity-scre.html

27 P I Ford, The negative-triangularity edge: heat-flux width, the ELM-free pedestal, and the scrape-off-layer boundary condition, Kronos Fusion Energy 2026 series. doi:10.5281/zenodo.22645830; https://www.kronosfusionenergy.com/publications/the-negative-triangularity-edge-heat-flux-width-the-elm.html

28 P I Ford, The Greenwald-fraction density limit and the radiative boundary: mapping the safe operating envelope of a compact spherical-tokamak breeder, Kronos Fusion Energy 2026 series. doi:10.5281/zenodo.22645947; https://www.kronosfusionenergy.com/publications/the-greenwald-fraction-density-limit-and-the-radiative-.html

29 P I Ford, First-wall and plasma-facing-component lifetime under 14 MeV loading, Kronos Fusion Energy 2026 series. doi:10.5281/zenodo.22645774; https://www.kronosfusionenergy.com/publications/first-wall-neutron-damage-lifetime.html

30 P I Ford, A stacked detachment portfolio for a compact spherical-tokamak breeder: Super-X, double-null and snowflake geometries that cut the required argon seed fraction, Kronos Fusion Energy 2026 series. doi:10.5281/zenodo.22645742; https://www.kronosfusionenergy.com/publications/divertor-portfolio.html

31 P I Ford, Real-time detachment control for a Super-X divertor in a compact spherical-tokamak breeder: radiated-power-fraction regulation with a radiative-collapse guard, Kronos Fusion Energy 2026 series. doi:10.5281/zenodo.22645874; https://www.kronosfusionenergy.com/publications/real-time-detachment-control-for-a-super-x-divertor-in-.html

32 P I Ford, *Kronos Physics De-Risking Register*, Kronos Fusion Energy 2026 series. doi:10.5281/zenodo.22133057

COLOPHON

How this document was made

The Kronos Fleet — Combined Editorial, 2026 is set in **Fraunces** (display), **Gelasio** (text), and **IBM Plex Mono** (data & equations), carried forward from the Kronos editorial design system.

The figures are rendered at 300 dpi from the deposited generator scripts; the document is composed as a single self-contained file with embedded fonts and imagery, paginated to US Letter, and rendered to PDF through a headless Chromium engine in matched light and dark editions.

Every headline quantity carries an evidence class; withdrawn and restated values are marked as such. Nothing herein is frozen beyond the founder-approved Tier-A set.

Explore it live — turn the interactive 3-D model, run the deposited solvers in the physics validator, and watch the companion film series.

LEGAL NOTICE

Notice, status, and distribution

Conceptual design & simulation study. This document reports a conceptual design and simulation study. It is not a construction commitment, a safety-analysis report, a regulatory filing, or an offer of securities. Forward-looking statements — schedules, costs, market sizes, and performance — are estimates subject to the limitations set out in the Simulations part and may change.

Numbers and their classes. Quantities are reported with evidence classes and case labels; modelled, assumed, and requirement-class values are identified as such and are not to be quoted without their labels.

Public edition. This edition carries the physics and design only; all financial, funding, and defense-commercial content has been removed for public distribution. The scientific text corresponds to the arXiv and journal submissions.

THE 2026 KRONOS SERIES

One programme, many papers

This editorial is one paper in the Kronos 2026 series — a real fusion company's complete, reproducible physics record for a spherical-tokamak breeder and its low-neutron D–^{3}He tandem-mirror burners. Every headline number is a frozen anchor in the Physics De-Risking Register.

Explore the whole programme: the De-Risking Register, the interactive 3-D model, and the physics validator.

KRONOS FUSION ENERGY

Collisional-Radiative Impurity-Radiation Modeling for a Compact Spherical-Tokamak Breeder: Closing the Core and Edge Radiated-Power Budget

A real fusion company building real machines. Explore the science, live.

Zenodo · doi:10.5281/zenodo.22645883

Read on kronosfusionenergy.com

The Physics De-Risking Register